Estimation of hydraulic conductivities using higher-order MRF-based stochastic joint inversion of hydrogeophysical measurements

Erasmus Kofi Oware[1]

Abstract

Stochastic imaging provides geologically realistic solutions to aquifer uncertainty quantification problems. Higher-order statistics for representing complex priors in stochastic-imaging problems are typically borrowed from training images, which may bias outcomes if the training images are unrepresentative of the desired structures. A Markov random field (MRF)-based stochastic-imaging algorithm, the spatial statistics of which are adaptively inferred directly from hydrogeophysical measurements without training images, is presented. For convenience of implementation, MRF models are commonly specified with pairwise interactions, limiting their ability to model complex architectures. MRF model specifications involving higher-order interactions are considered here. In the proposed algorithm, the lithologic structure of the aquifer and the hydraulic conductivities within the identified lithologies are simultaneously estimated in conformance to data-unconditioned and data-conditioned higher-order statistics while honoring the hydrogeophysical data sets. High reconstruction accuracy rates with nonsmooth, geologically realistic aquifer heterogeneities are reported in a hypothetical trinary hydrofacies aquifer characterization problem with various combinations of concentration and electrical-resistivity conditionings, illustrating the value of the different data types.

Introduction

Hydraulic conductivity (K) distributions exert the primary control on subsurface flow, which in turn drives subsurface transport, making the estimation of the spatial variations of K vitally important to subsurface resource (water and energy) management. While the traditional approach to estimating K, such as pumping tests, provides average K values over an entire aquifer, the accuracy of fine-scale K estimates from slug tests are limited to the immediate vicinity of the test well, limiting their ability to accurately predict large-scale transport behavior (Bohling et al., 2002). There is growing interest in the application of tomographic techniques such as hydraulic tomography (e.g., Yeh and Liu, 2000) and joint hydrogeophysical tomography (e.g., Rubin et al., 1992) for fine-scale descriptions of continuous K fields.

The tomographic problem can be formulated within a deterministic (e.g., Menke, 1984) or a stochastic framework (e.g., Vrugt, 2016). For uncertainty assessment and recovery of geologically realistic K architectures, the stochastic-imaging framework is preferred. Increasingly popular is the application of sequential geostatistical resampling (SGR) algorithms to represent complex prior models in stochastic-imaging problems (e.g., Ruggeri et. al., 2015; Linde et al., 2015). Higher-order simulations in SGR, however, are training-image-driven, making their recovered structures inextricably connected to the assumed patterns in the training images. Training images usually are constructed from ancillary data or expert information, which may bias realizations if the hypothesized features are unrepresentative of the target structures (e.g., Journel and Zhang, 2006). Thus, there is the need for data-driven higher-order modeling alternatives, especially, in the event of limited geologic context to construct reliable training images. The data-driven higher-order simulation (HOSIM) algorithm by Mustapha and Dimitrakopoulos (2010) is a classic example. Similarly, Tompkins et al. (2011) applied deterministic inversion of their data to estimate the mean and linearized covariance as priors for posterior sampling.

In an effort to further advance the development of data-driven higher-order simulation alternatives, an innovative data-driven stochastic-imaging scheme, Markov random field (MRF)-based stochastic imaging, is presented. MRF is a widely used spatial-modeling technique in image processing (e.g., Geman and Geman, 1984) and in medical imaging (e.g., Li et al., 1995). The traditional geostatistical approach to higher-order simulation borrows prior multiple-point statistics directly from training images (e.g., Mariethoz and Caers, 2014). Conditional estimation in MRF modeling, in contrast, leverages the equivalence of a Gibbs random field (GRF) and an MRF (Hammersley and Clifford, 1971) to identify probable local configurations in terms of their equivalent Gibbs energies. This approach to conditional estimation is convenient and practical (Derin and Elliott, 1987) if the parameters of the GRF (spatial statistics) are specified. The parameters of the GRF capture spatial statistical information, such as size, shape, orientation, clustering, and frequency of regions (Derin and Elliott, 1987).

The presented algorithm adaptively infers the parameters of the GRF from joint hydrogeophysical data sets without training images and subsequently applies the calibrated statistics for reconstruction. While Oware (2015) successfully tested the algorithm on a simple, binary hydrofacies hypothetical aquifer, here, the efficacy of the algorithm is demonstrated with a more complex, trinary hydrofacies synthetic aquifer. The review of higher-order models by Daly (2005) is of particular relevance to this contribution.

Theory and method

MRF-based conditional estimation. Conditional estimation in MRF modeling is based on neighborhood systems (NS) and their accompanying cliques. Li (2009) presents detailed descriptions of NS and cliques. Assume $\aleph$ is the NS of u (Figure 1a) within a pixelated domain Ω. A subset of $\aleph$, $c \subseteq \aleph$, defines a clique if every pair of distinct pixels in c are mutual neighbors (i.e., symmetric neighborhood). Figures 1b–1f show the 10 possible clique configurations associated with Figure 1a.

Suppose $\mathbf{k}$ is a realization of the random field (RF) $\mathbf{K}$. Then $\mathbf{K}$ is said to be a Markov random field (MRF) with respect to $\aleph$ if:

1) the joint probability $\Pr[\mathbf{k}] > 0 \; \forall \; \mathbf{k} \in \mathbf{K}$ (positivity property), and

[1]Department of Geology, SUNY at Buffalo.

http://dx.doi.org/10.1190/tle35090776.1.

2) the local conditional probabilities $\Pr[k(u)|\mathbf{k}(\aleph_u)]$ are defined $\forall\ u \in \Omega$ (Markov model), where $k(u)$ denotes the state at u and $\mathbf{k}(\aleph u)$ are the neighboring values of u. The local conditional probability can be expressed as:

$$\Pr\left[k(u)|\mathbf{k}(\aleph_u)\right]=\frac{\Pr\left[k(u),\mathbf{k}(\aleph_u)\right]}{\Pr\left[\mathbf{k}(\aleph_u)\right]}, \quad (1)$$

where $\Pr[k(u),\mathbf{k}(\aleph u)]$ and $\Pr[\mathbf{k}(\aleph u)]$ are the joint probabilities of the full template and the neighborhood configurations, respectively.

Specifying the MRF directly from conditional probabilities is, however, nontrivial since the joint distribution is not obvious and local characteristics of $\mathbf{K}$ are difficult to identify (Geman and Geman, 1984). The Hammersley-Clifford theorem (Hammersley and Clifford, 1971) establishes the equivalence of a Gibbs (or Boltzmann) distribution (GD) and a MRF (e.g., Daly, 2005). Derin and Elliott (1987) leveraged the theorem to express $\Pr[k(u),\mathbf{k}(\aleph u)]$ in terms of its GD equivalent and recast equation 1 as follows:

$$\Pr\left[k(u)|\mathbf{k}(\aleph_u),\theta\right]=\frac{e^{-V\left(k(u),\mathbf{k}(\aleph_u),\theta\right)}}{\Pr\left[\mathbf{k}(\aleph_u),\theta\right]}, \quad (2)$$

where $V(\bullet)$ is the potential function and θ is a vector containing the parameters of the GD. The evaluation of the denominator in equation 2, i.e., the normalization constant, is combinatorial requiring prior knowledge of all possible template configurations, rendering the computation of equation 2 infeasible. Traditionally, to facilitate the computation of equation 2, higher-order statistics are typically borrowed from training samples (e.g., Derin and Elliott, 1987; Strebelle, 2002).

To recall, the goal of this contribution is to provide a data-driven alternative to the generic training-image-based higher-order simulations. Since the denominator in equation 2 is a constant, the assessment of the conditional probability in equation 2 is dependent on only the numerator. Thus, Oware (2015) recasts equation 2 as a Bayesian inference problem as follows (e.g., Mosegaard and Tarantola, 1995):

$$\sigma(\mathbf{k})=c\rho(\mathbf{k})e^{-V\left(k(u),\mathbf{k}(\aleph_u),\theta\right)}, \quad (3)$$

where $\sigma(\bullet)$ and $\rho(\bullet)$ are the posterior and prior distributions, respectively; c is a normalization constant; and the potential function, $V(\bullet)$, assesses the likelihood of the unknown state given its neighboring values and a specified set of θ. The smaller the potential, the higher the likelihood of its associated configuration. Furthermore, Baye's theorem allows the integration of multiple observations (e.g., Irving and Singha, 2010) to further refine the conditional estimation. Therefore, typical data sets for conditioning the estimation of subsurface heterogeneities, such as hydraulic heads, $\mathbf{D}_{head}$, concentration, $\mathbf{D}_{conc}$, and geophysical, $\mathbf{D}_{geoph}$, measurements, for instance, can be incorporated into equation 3 to further refine the estimation. Mathematically,

$$\sigma(\mathbf{k})=c\rho(\mathbf{k})e^{-V\left(k(u),\mathbf{k}(\aleph_u),\theta\right)}L\left(\mathbf{D}_{head},\mathbf{D}_{conc},\mathbf{D}_{geoph}|\mathbf{k}\right), \quad (4)$$

where $L(\mathbf{D}_{head}, \mathbf{D}_{conc}, \mathbf{D}_{res}|\mathbf{k})$ is the joint likelihood of the hydrogeophysical measurements given $\mathbf{k}$. Indeed, equation 4 is at the heart of the presented algorithm.

Geologically realistic higher-order potential functions. The formulation of the potential function is crucial to the optimization procedure since it serves as a guide to searching for the minimal solution while providing a quantitative metric to assess the global quality of the solution (Li, 2009). While the parameterization of the clique potentials is arbitrary, its formulation is mostly application dependent. The Derin-Elliot MRF model expresses the potential function as a product of the pixel interaction intensities, ϕ, and the GD parameters, θ, i.e.,

$$V\left(k(u),\mathbf{k}(\aleph_u),\theta\right)=\phi^T\left(k(u),\mathbf{k}(\aleph_u)\right)\theta. \quad (5)$$

In a bid to reduce the number of cliques and the number of GD parameters to specify, MRF models are commonly formulated with cliques containing only one and two pixels, called pairwise pixel interaction (e.g., Oware, 2015). However, considering only pairwise interactions limits the ability of MRF to model complex patterns as those typically encountered in the geosciences. Consequently, higher-order interactions (e.g., Tjelmeland and Besag, 1998) involving cliques with more than two pixels (all cliques shown in Figure 1) are considered here. To construct the interaction intensity vector, ϕ, indicator functions are defined to assess how the pixels interact in the various cliques. Each element in ϕ, therefore, corresponds to a total interaction intensity due to one clique within $\aleph$. See Derin and Elliott (1987) for the complete formulation of their intensity vector.

It is important to attempt to formulate the potential function in a manner that ensures that the "correct solution" is embedded as the minimum, referred to as the correctness of the solution

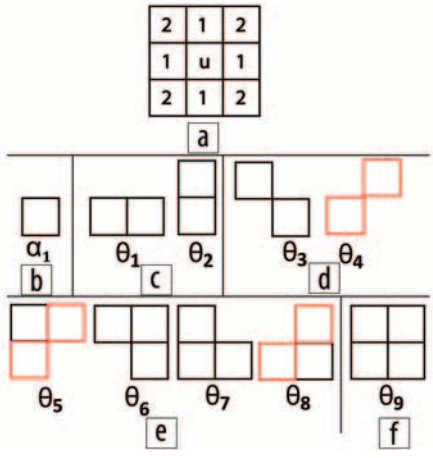

Figure 1. (a) Second-order neighborhood system; cliques: (b) single-site, (c) horizontal and vertical pair-site, (d) northwest-southeast and northeast-southwest diagonal pair-site, (e) triple-site, and (f) quadrupole-site. The θs represent the respective parameters of a Gibbs distribution (GD) of their corresponding clique. The red lines highlight diagonal members of the cliques oriented in the northeast-southwest direction to be discussed later.

(Li, 2009). Since the potential function is a product of the interaction intensities and the GD parameters, to aide in the "correct formulation," we can incorporate our prior understanding of the target system into the parameterization of the indicator functions, prior to estimating the GD parameters. Toward this end, the indicator functions here are designed to generate geologically realistic priors by encouraging clustering while retaining some level of randomness. It should be emphasized that lower potentials correspond to higher probabilities, and the reverse is true. To summarize the parameterization of the indicator functions, clique geometries consistent with the hypothesized patterns are promoted with the assignment of negative indicator values in order to drive down the estimated energy to increase the likelihood of acceptance, whereas clique configurations inconsistent with the theorized structures are penalized with positive indicator values to reduce their chances of acceptance. For instance, to encourage clustering with some level of randomness, clique geometries with two or more members belonging to the same state (lithology) with at least one dissimilar member are encouraged, whereas clique configurations with all dissimilar members are penalized in an attempt to reduce complete randomness in recovered structures.

Reconstruction algorithm. The reconstruction scheme is based on the two-step simulation approach (Deutsch and Journel, 1998) wherein the lithologic structure of the aquifer is modeled first, and the hydraulic conductivities (K) within identified lithologies are modeled second during each iteration (Figure 2). The two-step simulation approach produces results that are more consistent with the underlying physical phenomenon (e.g., sharp lithologic boundaries) and avoids extending the stationarity assumption underlying most continuous random field models (Deutsch and Journel, 1998). To summarize Figure 2, the primary simulation process (PSP) models the lithologic structure in the state space conditioned by the energy term in equation 4, whereas the secondary simulation process (SSP) simulates the K-space constrained by the joint likelihood term in equation 4.

Step 1 in Figure 2 estimates the prior statistics. Figure 3 outlines a proposed data-driven adaptive algorithm to implicitly infer the GD parameters based on equation 4. First, prior GD parameters are employed to perform the reconstruction (i.e., Figure 2) until a user-defined number of consecutive rejections of the reconstructed image is attained, after which the GD parameter space is resimulated. The number of consecutive rejections was set to three in this implementation. The set of GD parameters that produced an accepted reconstruction is saved as a sample of the posterior GD parameter distribution. The consecutive rejection count is reset to zero after each acceptance. The process continues iteratively until a user-defined number of posterior GD parameters is sampled.

A hybrid of the Gibbs sampler was used for the PSP. In the conventional Gibbs sampler, the value at a visited node is renewed according to its neighboring values and the imposed statistical structure without rejection (Geman and Geman, 1984). The lack of rejection limits the ability of the Gibbs sampler to model complex systems (Tarantola, 2005). Thus, a modification of the Gibbs sampler that incorporates rejection was used to leverage

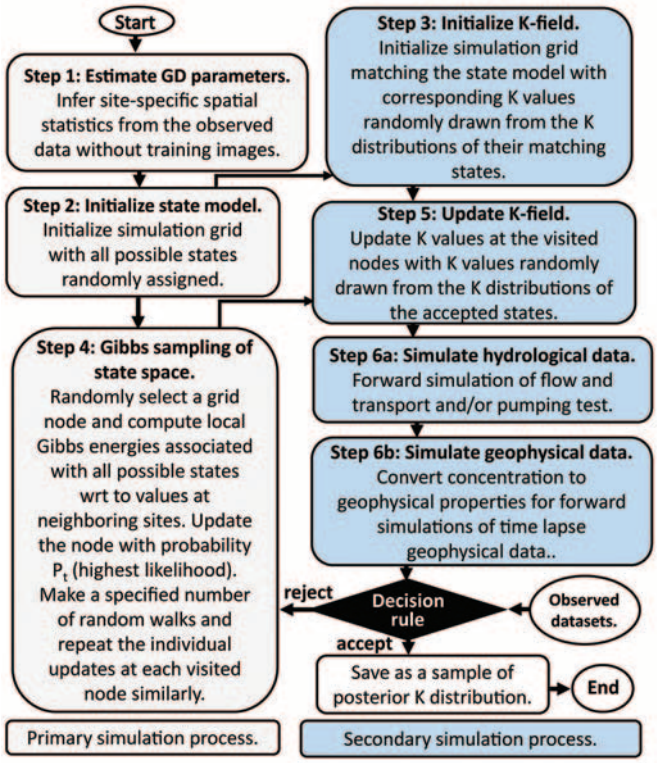

Figure 2. Flowchart of the computational algorithm.

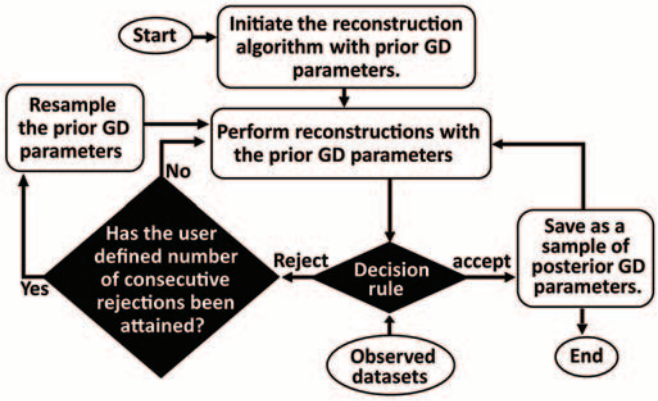

Figure 3. Data-driven adaptive algorithm to estimate site-specific GD parameters.

the computational efficiency of the Gibbs sampler (e.g., Mosegaard and Sambridge, 2002) and the robustness of the Metropolis algorithm (Metropolis et al., 1953; Hastings, 1970) to model complex problems.

Numerical experiments. The algorithm is demonstrated with cross-borehole conservative solute transport experiments coupled with electrical-resistivity (ER) monitoring in a trinary hydrofacies hypothetical aquifer (Figure 4). The target domain is a 16 m × 8 m depth cross-section discretized into 0.25 m × 0.25 m cells producing a 64 × 32 simulation grid. To simulate the trinary hydrofacies aquifer, Sequential Gaussian Simulation (SGSIM) program from the GSLIB (Deutsch and Journel, 1998) was first applied to generate a highly heterogeneous random field with northwest-southeast dipping of features. The RF was then

parameterized into three categories, producing a trinary hydrofacies structure. Since the distributions of hydraulic conductivities (K) in lithologic units are approximately lognormal (e.g., Freeze, 1975), lognormal distributions with mean K values of 10 m/d, 30 m/d, and 100 m/d were simulated within facies 1, facies 2, and facies 3, respectively. Log standard deviation of 0.1 was assumed for all facies. Mean of K can be estimated easily from pumping or slug tests, hence, mean K values of the facies were assumed known during the reconstruction whereas the log standard deviation was set to 0.12 to account for uncertainty in estimating the range of K values in field applications.

Figure 4 provides a conceptual model of the flow and transport experiment. Steady-state flow was simulated with no-flow boundaries assumed for the top and bottom boundaries with constant-head boundaries imposed at the left and right ends. A lateral pressure difference of about 1 Pa was imposed between the two lateral ends. To simulate transport, a 1000 mg/L conservative saline tracer was continuously injected along the full column of bh1 (e.g., Irving and Singha, 2010) within a background of 10 mg/L. The resulting concentration field was monitored every 4 hours for 8 days resulting in a total of 48 time-steps. Concentration breakthroughs for each time-step were sampled in a multilevel array of 16 sampling ports located in only bh2. All the synthetic tracer experiments were simulated using a MATLAB-based flow and transport simulation program, MatFlot (Künze and Lunati, 2012).

For the ER monitoring, all the concentration distributions were converted into 48 ER snapshots. First, the solute concentrations, **C** (mg/L), were converted into fluid resistivities, $\boldsymbol{\rho}_f$ (ohm.m) (Keller and Frischknecht, 1966):

$$\boldsymbol{\rho}_f = 500/\mathbf{C}.$$

Afterward, $\boldsymbol{\rho}_f$ were converted into bulk resistivities, $\boldsymbol{\rho}_b$, according to (Archie, 1942):

$$\boldsymbol{\rho}_b = \boldsymbol{\rho}_f n^{-m},$$

where n represents porosity, which was set to constant values of 0.1, 0.2, and 0.3 for facies 1, facies 2, and facies 3, respectively; m denotes the cementation factor, which was set to 1.3 representing unconsolidated materials (e.g., Knight and Endres, 2005). Petrophysical conversion uncertainties, such as the spatial variability of m, petrophysical scaling effects (e.g., Moysey et al., 2005), and surface conduction as a result of the presence of fine particles were considered negligible.

In the ER survey, 81 electrodes were deployed comprising 17 surface electrodes and 32 borehole electrodes in each well with 0.5 m spacing between all electrodes. Circulating dipole-dipole (e.g., Slater et. al., 2000) data collection routine was employed to acquire a total of 225 surface and 5630 cross-borehole quadrupole measurements at the end of each time-step's resistivity data acquisition. All resistivity forward simulations and sampling were performed using a Matlab-based resistivity modeling code, FW2_5D (Pidlisecky and Knight, 2008). Both concentration and ER measurements were corrupted with white Gaussian noise with standard deviations proportional to 3% of the data values.

Results and discussions

It was assumed in the reconstructions that facies values at borehole locations are easily obtainable from rock cores or optical borehole images. Accordingly, the true facies values at well locations were inserted at their respective positions in the simulation grid and their values frozen throughout all reconstructions. To

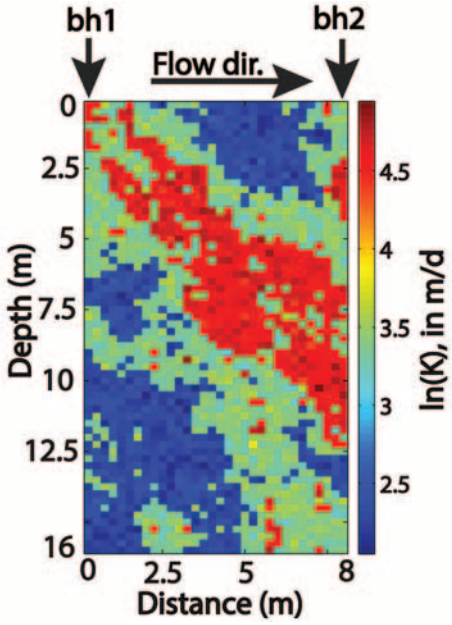

Figure 4. Log of hydraulic conductivities of the trinary hydrofacies aquifer: synthetic target. Borehole locations: 1 (bh1), and 2 (bh2).

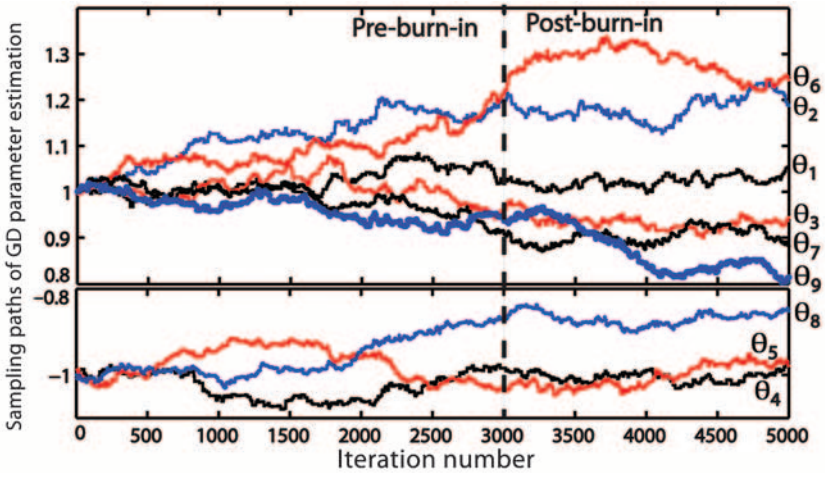

Figure 5. Sampling paths of GD parameter estimation for 5000 iterations. The broken line marks the burn-in time. The GD parameter labels corresponding to the curves are displayed on the right axis (see Figure 1 for their matching clique configurations).

estimate the GD parameters, the adaptive algorithm was run for 5000 iterations, with each iteration comprising 1000 random walks (step-size). The starting model for all reconstructions is an unconditionally generated random field containing all three possible states. No knowledge of the prior GD parameter structure was assumed; hence, they were all set to one (Figure 5).

It was observed from multiple test runs, however, that the polarities of the GD parameters control orientation of features. Consequently, different combinations of their polarities were tested to identify the optimal combination that generates patterns that minimize the joint data sets consistently, especially polarity combination that creates structures with high acceptance rate during the first few iterations. After identifying the appropriate mix of the polarities, it was discovered that all the cliques with negative GD parameters (i.e., θ_4, θ_5, and θ_8) contain two pixels (highlighted in red in Figure 1) oriented in the northeast-southwest diagonal direction. The northeast-southwest inclination of those clique pixels is opposite (i.e., about 90° rotation) to the general orientation of features in the target (Figure 4), suggesting that GD parameters of some specific clique geometries can be negated to rotate features in a preferred direction.

The GD parameter estimation reached an equilibrium level after about 3000 iterations (Figure 5). The estimated means of the post-burn-in GD parameters for θ_1, θ_2, θ_3, θ_4, θ_5, θ_6, θ_7, θ_8, and θ_9, respectively, were 1.02, 1.18, 0.93, -1.00, -1.05, 1.28, 0.90, -0.87, and 0.88. The proximity of the estimated means to the prior values indicates that the starting values of ones were close to the mode of most of the posterior GD parameter distributions. The posterior means were subsequently applied as calibrated statistics for the full reconstruction.

The reconstruction was initiated with a step-size of 1000 random walks per iteration for the first 1000 iterations to allow the algorithm to burn in rapidly and establish the large-scale structures quickly. After that, the step-size was reduced to 100 per iteration for the remaining iterations, to enable the recovery of small-scale details. To assess the ability of the algorithm to perform reconstruction independent of the "soft" data calibrated GD parameters, the reconstruction was first performed with all the GD parameters set to one with the optimal polarity combination. In that case, the inversion was based on only the prior spatial statistical information captured in the parameterization of the indicator functions.

This scenario was considered for three different data conditionings of concentration only, resistivity only, and joint concentration and resistivity. Analyses of the sampling paths of the likelihoods (not shown) reveal that the algorithm burned in after about only 500 iterations. The posterior analyses involved at most 1000 samples from iterations 1000 to 2000, when the step-size was reduced to a constant value of 100 pixel updates per iteration. Performing autocorrelation analysis to determine statistically independent posterior samples was not considered. The mean and standard deviations of the posterior samples alongside three realizations for the inversions of concentration only, resistivity only, and joint concentration and resistivity are, respectively, displayed in Figures 6, 7, and 8.

Comparison of the mean estimate with the target for the concentration-only conditioning (Figure 6) indicates that all the large-scale structures of the aquifer were fairly identified even though the concentration sampling ports were located in only bh2. Examination of the standard-deviation plot reveals high uncertainty associated with the delineation of lithologic boundaries and the low-K (facies 1) patch near the surface. The three realizations at iterations 1000, 1500, and 2000 appear independent and identical, revealing poor resolution of features in the midsection of the domain where there is poor data sensitivity.

The resistivity-only conditioning (Figure 7) recovered improved resolution of features in contrast to those obtained from concentration only due to the spatially continuous sensitivity of resistivity measurements. However, the short strip of facies 2 at the top left corner and the scattered facies 2 within the high-K channel in the target created an artifact of a strip of facies 2 within the recovered high-K channel. Similarly, the facies 1 spot at the bottom right corner was linked to the patch of facies 1 at the top, creating a linear artifact. While the resistivity-only conditioning identified the isolated piece of facies 2 in the bottom left corner of the domain, it failed to detect the patch of facies 1 near the surface, which plausibly stems from the inherent poor cross-borehole resistivity resolution near the surface coupled with MRF degeneracy. Note that the bulk of the resistivity measurements was a cross-borehole acquisition. The strips of artifacts were captured as high-uncertainty lineation in the standard-deviation panel. The three realizations depict the sharpness and the geologically realistic nature of the recovered lithologic boundaries.

The combination of the concentration and resistivity data sets in the joint inversion (Figure 8) retrieved fewer artifacts and improved resolution of attributes in contrast to those obtained from the individual data sets, demonstrating the synergistic benefits of joint inversion. While the joint inversion resolved the patch of facies 1 near the surface, it failed to detect the isolated piece of facies 2 at the bottom left corner, which was identified in the resistivity-only inversion, suggesting that the composite resolution of joint inversion may not always result in improved estimation of small-scale details.

Only at most 2000 iterations were considered because the reconstruction degenerates after about 2000 iterations. MRF degeneracy occurs when long-range correlations are constructed as the reconstruction progresses, resulting in undesirable large patches of one-state (e.g., Besag, 1986). The early onset of degeneracy here is attributable to the nonspecificity of the GD parameters. Nonetheless, the ability of the algorithm to resolve the large-scale structures without site-specific GD parameters demonstrates the efficacy of the presented algorithm and the potential of capturing prior information into the formulation of the indicator functions. Furthermore, the process of performing reconstruction with all the GD parameters set to one can be applied as a guide in parameterizing the indicator functions, to ensure that the indicator functions generate structures that are somehow consistent with our prior expectation.

The utilization of the site-specific statistics improves the reconstruction and seems to extend the onset of degeneracy slightly. For the sake of brevity, results of only the joint inversion are presented for the site-specific statistics case. The posterior analyses comprise samples from iterations 1500 to 3300. The mean and standard deviations of the posterior samples alongside three

realizations are presented in Figure 9. All the large-scale structures were once again identified, with improved estimation of the thickness of the high-K channel in contrast to results obtained from the inversions without site-specific statistics. Small-scale features, however, were not properly resolved, particularly, the patch of facies 1 around the 7.5 m depth near bh1. This misidentification is plausibly ascribable to the 4 hours temporal resolution, which seems inadequate to detect fine-scale details near the injection well where features get inundated quickly with the tracer at the beginning of injection. A potential solution to this problem is to include background measurements in the time-lapse data set, which was unintentionally omitted here. The standard-deviation panel indicates high uncertainty related to the identification of lithologic boundaries. Visual inspection of the three realizations at iterations 2000, 2500, and 3000 discloses increasing extent of the two facies 1 regions as the number of iterations progresses, which is an evidence of degeneracy. While degeneracy appears to be a limitation we nevertheless obtain seemingly acceptable posterior samples before the reconstruction degenerates.

It takes about only 2.5 hours to complete the inversion without site-specific GD parameters. The GD parameter estimation and the reconstruction with site-specific statistics require about 6.5

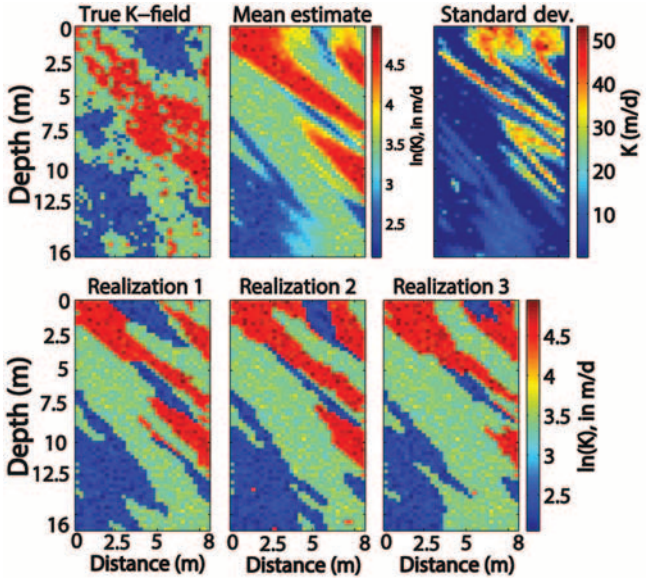

Figure 6. Tomograms of concentration only without site-specific GD parameters. Row 1 shows the true K-field (column 1), mean estimate (column 2), and standard deviation (column 3); row 2 shows samples of realizations at iterations: 1000 (column 1), 1500 (column 2), and 2000 (column 3).

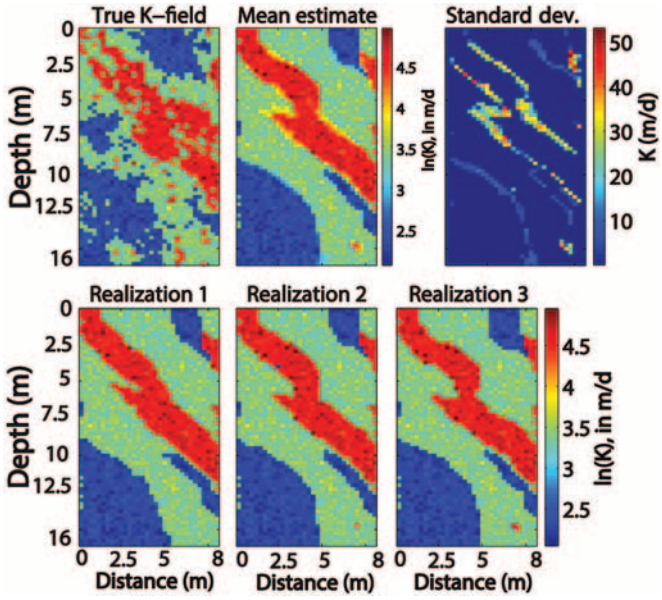

Figure 8. Tomograms of joint concentration and resistivty without site-specific GD parameters. Row 1 shows the true K-field (column 1), mean estimate (column 2), and standard deviation (column 3); row 2 shows samples of realizations at iterations: 1000 (column 1), 1300 (column 2), and 1600 (column 3).

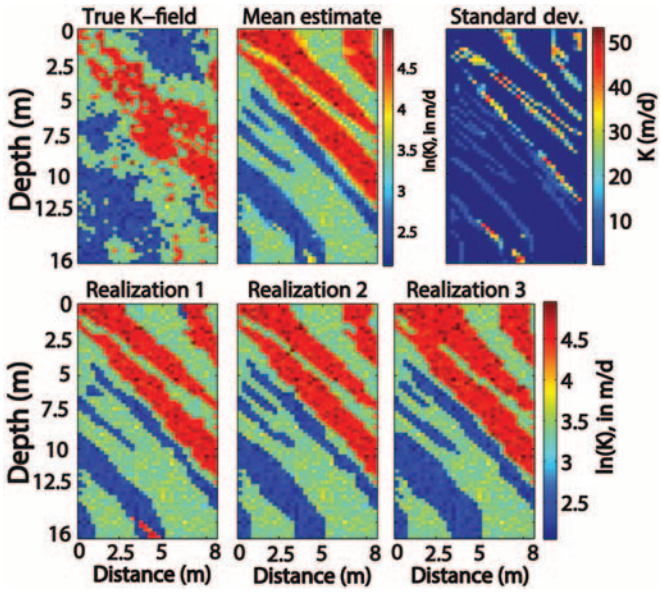

Figure 7. Tomograms of resistivity only without site-specific GD parameters. Row 1 shows the true K-field (column 1), mean estimate (column 2), and standard deviation (column 3); row 2 shows samples of realizations at iterations: 1000 (column 1), 1500 (column 2), and 2000 (column 3).

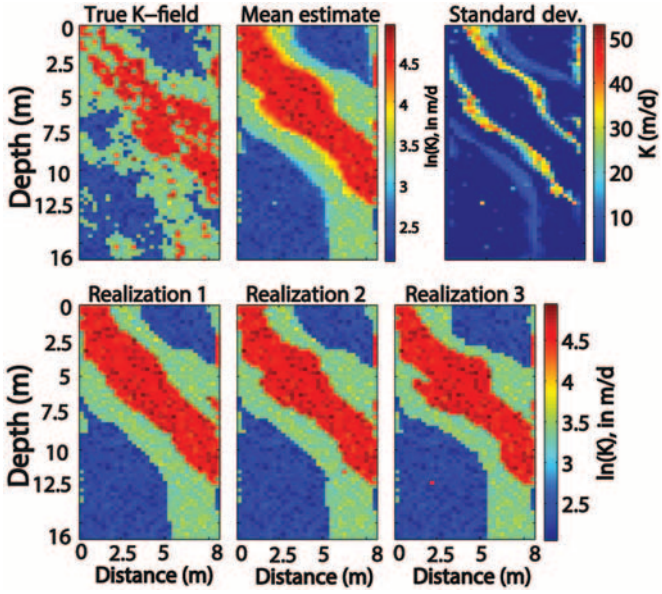

Figure 9. Tomograms of joint concentration and resistivty with site-specific GD parameters. Row 1 shows the true K-field (column 1), mean estimate (column 2), and standard deviation (column 3); row 2 shows samples of realizations at iterations: 2000 (column 1), 2500 (column 2), and 3000 (column 3).

hours and 3.5 hours of computational time, respectively. The inversions were performed on a desktop computer with 2.6 GHz dual processors and 32 GB RAM with six cores. The seemingly high computational efficiency stems from the rapid convergence of Gibbs sampling (e.g., Mosegaard and Sambridge, 2002), meaning a limited number of hydrogeophysical forward simulations are needed before obtaining samples of the posterior distribution.

Conclusions

A Markov random field (MRF)-based stochastic joint inversion of hydrogeophysical data sets to estimate continuous spatial variations of hydraulic conductivities (K) was presented. The proposed strategy captures site-specific spatial statistics in the form of parameters of a Gibbs distribution (GD) from conditioning data sets, and subsequently applies the calibrated GD parameters to simulate structural patterns representative of the study site. Reconstructions without site-specific statistics were also considered.

High reconstruction accuracy rates with nonsmooth, geologically realistic lithologic boundaries were recovered. The algorithm burns-in rapidly, presenting a viable approach to improving the computational efficiency of stochastic-imaging problems. One of the main challenges of the application of MRF-based modeling in the geosciences is that, as in image processing, some operation has to be performed on the complete image (Mariethoz and Caers, 2014), especially the estimation of the statistical parameters. Since the "entire" subsurface is inaccessible in the applications considered here, the presented adaptive algorithm to calibrate the GD parameters from joint hydrogeophysical measurements sheds new light on this long-standing challenge. Additionally, the ability of the strategy to reconstruct a target based on limited prior information without site-specific statistics looks encouraging. Indeed, for the GD parameters to be independent of soft data, they can also be inferred from training images (e.g., Derin and Elliott, 1987) if enough ancillary data and sound geologic context are available to construct reliable training images.

While the results presented here seem appealing and promising, further research is needed to fully understand the behavior of the algorithm for specific applications of interest in the geosciences. Specifically, further research is required to advance the concept of data-driven estimation of GD parameters and to improve the parameterization and formulation of MRF models for a fully nondegenerate condition. TLE

Corresponding author: erasmuso@buffalo.edu

References

Archie, G. E., 1942, The electrical resistivity log as an aid in determining some reservoir characteristics: Transactions of the American Institute of Mining, Metallurgical and Petroleum Engineers, **146**, 54–62, http://dx.doi.org/10.2118/942054-G.

Besag, J., 1986, On the statistical analysis of dirty pictures: Journal of the Royal Statistical Society. Series B. Methodological, **48**, no. 3, 259–302.

Bohling, G. C., X. Zhan, J. J. Butler Jr., and L. Zheng, 2002, Steady shape analysis of tomographic pumping tests for characterization of aquifer heterogeneities: Water Resources Research, **38**, no. 12, 60-1–60-15, http://dx.doi.org/10.1029/2001WR001176.

Daly, C., 2005, Higher order models using entropy, Markov random fields and sequential Simulation: Geostatistics-Banff: Kluwer Academic Publications.

Derin, H., and H. Elliott, 1987, Modeling and segmentation of noisy and textured images using gibbs random fields: IEEE Transactions on Pattern Analysis and Machine Intelligence, **PAMI-9**, no. 1, 39–55, http://dx.doi.org/10.1109/TPAMI.1987.4767871.

Deutsch, C. V., and A. G. Journel, 1998, GSLIB: Geostatistical Software Library and User's Guide: Oxford Univ. Press.

Freeze, R. A., 1975, A stochastic-conceptual analysis of one-dimensional groundwater flow in nonuniform homogeneous media: Water Resources Research, **11**, no. 5, 725–741, http://dx.doi.org/10.1029/WR011i005p00725.

Geman, S., and D. Geman, 1984, Stochastic relaxation, gibbs distributions, and the bayesian restoration of images: IEEE Transactions on Pattern Analysis and Machine Intelligence, **PAMI-6**, no. 6, 721–741, http://dx.doi.org/10.1109/TPAMI.1984.4767596.

Hammersley, J. M., and P. Clifford, 1971, Markov fields on finite graphs and lattices: Unpublished manuscript, Oxford University.

Hastings, W., 1970, Monte Carlo sampling methods using Markov chains and their applications: Biometrika, **57**, no. 1, 97–109, http://dx.doi.org/10.1093/biomet/57.1.97.

Irving, J. D., and K. Singha, 2010, Stochastic inversion of tracer test and electrical geophysical data to estimate hydraulic conductivities: Water Resources Research, **46**, no. 11, W11514, http://dx.doi.org/10.1029/2009WR008340.

Journel, A., and T. Zhang, 2006, The necessity of a multiple-point prior model: Mathematical Geology, **38**, no. 5, 591–610, http://dx.doi.org/10.1007/s11004-006-9031-2.

Keller, G. V., and F. C. Frischknecht, 1966, Electrical Methods in Geophysical Prospecting: Pergamon.

Knight, R. J., and A. L. Endres, 2005, An introduction to rock physics for near-surface applications, *in* D. K. Butler, ed., Near-surface geophysics: SEG, Investigations in Geophysics, 31–70, http://dx.doi.org/10.1190/1.9781560801719.ch3.

Künze, R., and I. Lunati, 2012, An adaptive multiscale method for density-driven instabilities: Journal of Computational Physics, **231**, no. 17, 5557–5570, http://dx.doi.org/10.1016/j.jcp.2012.02.025.

Li, S. Z., 2009, Markov random field modeling in image analysis: Springer Science & Business Media.

Li, H. D., M. Kallergi, L. P. Clarke, V. K. Jain, and R. A. Clark, 1995, Markov random field for tumor detection in digital mammography: IEEE Transactions on Medical Imaging, **14**, no. 3, 565–576, http://dx.doi.org/10.1109/42.414622.

Linde, N., P. Renard, T. Mukerji, and J. Caers, 2015, Geological realism in hydrogeological and geophysical inverse modeling: A review: Advances in Water Resources, **86**, 86–101, http://dx.doi.org/10.1016/j.advwatres.2015.09.019.

Mariethoz, G., and J. Caers, 2014, Multiple-point geostatistics: Stochastic modeling with training images: John Wiley & Sons.

Menke, W., 1984, Geophysical data analysis: Discrete Inverse Theory: Academic Press.

Metropolis, N., A. W. Rosenbluth, M. N. Rosenbluth, A. H. Teller, and E. Teller, 1953, Equation of state calculations by fast computing machines: The Journal of Chemical Physics, **21**, no. 6, 1087–1092, http://dx.doi.org/10.1063/1.1699114.

Mosegaard, K., and M. Sambridge, 2002, Monte Carlo analysis of inverse problems: Inverse Problems, **18**, no. 3, R29–R54, http://dx.doi.org/10.1088/0266-5611/18/3/201.

Mosegaard, K., and A. Tarantola, 1995, Monte Carlo sampling of solutions to inverse problems: Journal of Geophysical Research, **100**, B7, 12431–12447, http://dx.doi.org/10.1029/94JB03097.

Moysey, S. M. J., K. Singha, and R. Knight, 2005, A framework for inferring field-scale rock physics relationship through numerical simulation: Geophysical Research Letters, **32**, no. 8, L08304, http://dx.doi.org/10.1029/2004GL022152.

Mustapha, H., and R. Dimitrakopoulos, 2010, High-order stochastic simulation of complex spatially distributed natural phenomena: Mathematical Geosciences, **42**, no. 5, 457–485, http://dx.doi.org/10.1007/s11004-010-9291-8.

Oware, E. K., 2015, Bayesian Gibbs Markov chain: MRF-based stochastic joint inversion of hydrological and geophysical datasets for improved imaging of aquifer heterogeneities: Abstract #H H13E 1591, 2015 Fall Meeting, AGU, San Francisco, Dec. 2015.

Pidlisecky, A., and R. J. Knight, 2008, FW2_5D: A MATLAB 2.5-D electrical resistivity modeling code: Computers & Geosciences, **34**, no. 12, 1645–1654, http://dx.doi.org/10.1016/j.cageo.2008.04.001.

Rubin, Y., G. Mavko, and J. Harris, 1992, Mapping permeability in heterogeneous aquifers using hydrologic and seismic data: Water Resources Research, **28**, no. 7, 1809–1816, http://dx.doi.org/10.1029/92WR00154.

Ruggeri, P., J. Irving, and K. Holliger, 2015, Systematic evaluation of sequential geostatistical resampling within MCMC for posterior sampling of near-surface geophysical inverse problems: Geophysical Journal International, **202**, no. 2, 961–975, http://dx.doi.org/10.1093/gji/ggv196.

Slater, L., A. M. Binley, W. Daily, and R. Johnson, 2000, Cross-hole electrical imaging of controlled saline tracer injection: Journal of Applied Geophysics, **44**, no. 2-3, 85–102, http://dx.doi.org/10.1016/S0926-9851(00)00002-1.

Strebelle, S., 2002, Conditional simulation of complex geological structures using multiple point statistics: Mathematical Geology, **34**, no. 1, 1–21, http://dx.doi.org/10.1023/A:1014009426274.

Tarantola, A., 2005, Inverse problem theory and methods for model parameter estimation: Society of Industrial and Applied Mathematics.

Tjelmeland, H., and J. Besag, 1998, Markov Random Fields with Higher-order Interactions: Scandinavian Journal of Statistics, **25**, no. 3, 415–433, http://dx.doi.org/10.1111/1467-9469.00113.

Tompkins, M. J., J. L. Fernández Martínez, D. L.Alumbaugh, and T. Mukerji, 2011, Scalable uncertainty estimation for nonlinear inverse problems using parameter reduction, constraint mapping, and geometric sampling: Marine controlled-source electromagnetic examples. Geophysics, **76**, no. 4, F263–F281, http://dx.doi.org/10.1190/1.3581355.

Vrugt, J. A., 2016, Markov chain Monte Carlo simulation using the DREAM software package: Theory, concepts, and MATLAB implementation: Environmental Modelling & Software, **75**, 273–316, http://dx.doi.org/10.1016/j.envsoft.2015.08.013.

Yeh, T. C. J., and S. Liu, 2000, Hydraulic tomography: Development of a new aquifer test method: Water Resources Research, **36**, no. 8, 2095–2105, http://dx.doi.org/10.1029/2000WR900114.